Capsule-train stability

Spencer H. Bryngelson[1] and Jonathan B. Freund[1,2,*]

[1]*Department of Mechanical Science & Engineering, University of Illinois at Urbana–Champaign,*
Urbana, Illinois 61801, USA
[2]*Department of Aerospace Engineering, University of Illinois at Urbana–Champaign,*
Urbana, Illinois 61801, USA

Elastic capsules flowing in small enough tubes, such as red blood cells in capillaries, are well known to line up into regular single-file trains. The stability of such trains in somewhat wider channels, where this organization is not observed, is studied in a two-dimensional model system that includes full coupling between the viscous flow and suspended capsules. A diverse set of linearly amplifying disturbances, both long-time asymptotic (modal) and transient (nonmodal) perturbations, is identified and analyzed. These have a range of amplification rates and their corresponding forms are wavelike, typically dominated by one of five principal perturbation classes: longitudinal and transverse translations, tilts, and symmetric and asymmetric shape distortions. Finite-amplitude transiently amplifying perturbations are shown to provide a mechanism that can bypass slower asymptotic modal linear growth and precipitate the onset of nonlinear effects. Direct numerical simulations are used to verify the linear analysis and track the subsequent transition of the regular capsule trains into an apparently chaotic flow.

I. INTRODUCTION

Red blood cells or similar elastic capsules suspended in sufficiently small vessels or tubes are well known to flow in single-file trains down the center of the vessel, each assuming a bullet-like [1,2] or sometimes asymmetric slipper-like [3–7] shape. Such a regular formation would seem viable in larger tubes or vessels, yet this is not observed for long times, presumably because it is unstable. What is observed instead is a significantly disturbed flow, in which capsules or blood cells appear to flow chaotically relative to each other in addition to their predominantly streamwise advection [2,8–10]. This empirical behavior has been reproduced in detailed numerical simulations [11–14], such as those visualized in Fig. 1. It is well known that purely viscous flows can display chaotic streamlines, such as in two-dimensional mixing configurations [15,16] and certain three-dimensional bounded flows [17–19]. Further, viscous N-body systems can also display chaos. A free-space Stokeslet model suggests that $N = 3$ is sufficient [20] and chaos has indeed been observed for three rigid spheres suspended within a rotating cylinder [21]. So it is not surprising that this transition can occur; we consider specifically when and how it manifests for flexible capsules in a model channel.

The source of this instability is unknown, particularly in how it might be affected by capsule properties or flow configurations, which can be altered, for example, by disease in red blood cells. In addition to the basic role of blood cells in transport through the microcirculation [22,23], many important microcirculatory flows are potentially sensitive to this change in character: the cell-free layers that form near vessel walls [24–26], the margination of leukocytes or platelets [27–31], intravenous drug delivery of particles and capsules for which both cross-stream transport and the thickness of the near-wall cell-free layer can be important [32], the hemodynamic forces that mediate angiogenesis [33] and development [32,34,35], and tumor growth in cancer [36]. Capsule-train stability is potentially even more important for microfluidic devices designed to manipulate the

---

*jbfreund@illinois.edu
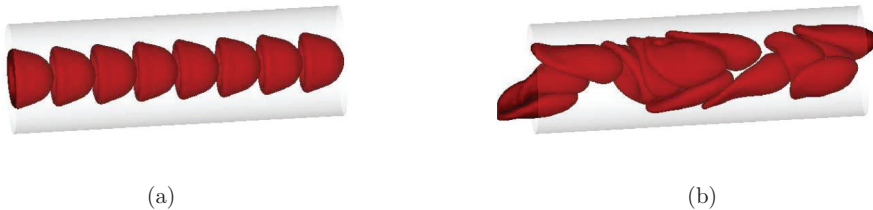
(a)   (b)

FIG. 1. Empirical stability example for red blood cells using methods of Zhao *et al.* [11]: (a) stable and (b) unstable. Both configurations were equally perturbed, but the $N = 8$ cell train in (a) seems to persist indefinitely, whereas the more dense $N = 12$ case in (b) undergoes a rapid transition. This shows a sensitivity to packing fraction in addition to diameter sensitivity discussed in the text.

flow of cells or engineered capsules in order to perform sorting or other processing [37–42]. In such devices, it is seemingly easiest to develop processing procedures that operate on ordered trains rather than chaotic and disperse arrangements.

We focus on the character of the transition between the orderly flow, typically seen in the narrowest tubes or vessels [1,43], and its apparently chaotic counterpart, typically seen in less confined configurations [44,45]. Our goal is to identify factors mediating its transition, the rate at which disturbances amplify, and the character of the most-amplifying disturbances. A two-dimensional flow of uniformly spaced capsules, which empirically displays this threshold behavior, is analyzed as a model system. While there is no expectation that this model provides a quantitative description of any particular three-dimensional configuration, such as true blood cells, it is more amenable to extensive analysis. We will see that it displays a rich range of behaviors that are suggestive of the potential diverse behaviors possible in similar systems. The specific configuration is introduced in Sec. II. The numerical methods used both for constructing the linearization and for the corresponding direct numerical simulations (DNSs) are summarized in Sec. III.

To analyze stability of the capsule trains, both eigensystem and singular-value analyses of the linearized system are use to predict the asymptotic and transient behaviors of perturbations, respectively. The formulation for this is outlined in Sec. IV, following a similar approach to that used to analyze shear-flow instability at larger Reynolds numbers [46–49]. Here these methods are adapted to the fluid-structure coupled system in the viscous-flow limit. Direct numerical simulations for specific cases confirm both the predicted transient and asymptotic amplification rates and show the subsequent nonlinear evolution of the system away from the ordered configuration.

The present analysis is in the same spirit as stability analyses of settling lines of spheres in free space [50,51] or near a wall [52], which is analytically tractable in the limit of infinitesimal spheres, though often by neglecting interactions beyond nearest neighbors. While similar in character to these simpler configurations, the present study includes all viscous-flow interactions, including the coupled elastic stresses in the deformable capsule membranes. This complexity necessitates some reliance upon numerical methods, though the stability results themselves are relatively clear. Similar nonmodal stability analysis has been used to study rheologically complex flows [53], but does not appear to have been used to analyze the behavior of confined particle suspensions, such as that which we consider here with flexible capsules. Observational studies of one-dimensional droplet arrays have also been conducted that display some superficial similarities to our study of elastic capsules [54–56]; however, it appears that fundamental differences between droplets and capsules, specifically, the presence of an elastic membrane, seemingly limit a qualitative connection [57].

Amplification rates and corresponding most-amplifying disturbances for relatively wide and narrow channels with both large and small capsule-packing fractions are summarized in Sec. V. These perturbations are examined in regard to the transition to nonlinear behavior in Sec. VI, which includes DNSs of their evolution into an apparently chaotic flow. Small disturbances that are particularly subject to transient growth—the nominally "most dangerous" disturbances often discussed for boundary layers [58–60]—are shown to lead to nonlinearity and chaos as much as
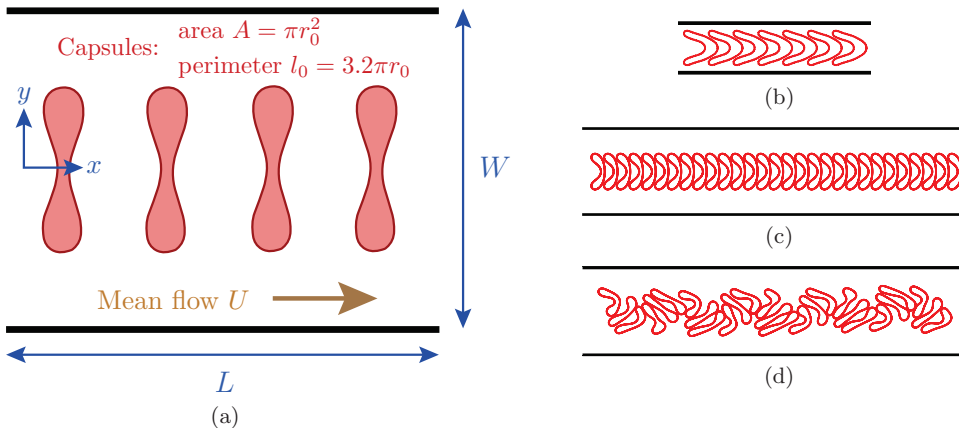
FIG. 2. (a) Schematic of the model channel flow with mean flow U containing N capsules of area $A = \pi r_0^2$ and perimeter $l_0 = 1.6 \times 2\pi r_0$. (b) Empirically stable single-file train in a narrow $W = 4r_0$ channel, (b) empirically unstable train in a $W = 10r_0$ channel, and (d) transition of (c) into an apparently chaotic flow.

1000 times faster than the most asymptotically unstable disturbance. For efficient design of devices and methods that maintain organization by avoiding instabilities, it is essential to consider such disturbances, as has also been recognized in other flows [61–65]. *Ad hoc* random perturbations of the same displacement amplitude grow much more slowly, suggesting that the specific most-amplifying disturbances are of principal importance. Capsule-train stability is shown to be sensitive to capsule flexibility in Sec. VII, where we also investigate the deformation energy that accompanies the different disturbances.

II. MODEL MICROCHANNEL

The model capsule-flow system is shown in Fig. 2. A streamwise-periodic channel of length L and width W contains N capsules suspended in a viscosity μ Newtonian fluid flowing with mean speed U. Each capsule has area $A = \pi r_0^2$ and a zero-stress perimeter $l_0 = 1.6 \times 2\pi r_0$ such that its biconcave equilibrium geometry is similar to the cross section of a resting red blood cell. The capsules are initialized in their at-rest equilibrium geometry and uniformly spaced along the channel centerline in a one-dimensional train with packing fraction

$$\phi \equiv \frac{N r_0}{L}, \tag{1}$$

which is varied from dilute $\phi = 0.2$ to nearly jammed $\phi = 0.7$. Most results are presented for the relatively narrow $W = 10r_0$ and wide $W = 40r_0$ channels visualized in Fig. 3. Channel lengths are varied from $L = 10r_0$ to $500r_0$, with the number of capsules correspondingly varied from $N = 2$ to 100. Results will show that an apparent asymptotic large-L behavior is achieved for $N \gtrsim 20$, which motivates particular focus on cases with $N = 30$. We restrict our investigation to this ordered and regular capsule train, such as that which might be generated by more narrowly confining upstream geometries. No attempt is made to identify stable states that might exist in wide channels, such as those apparently seen in some staggered arrays of immiscible droplets [54].

Each capsule is defined as an elastic shell that resists tension and bending with linear moduli $\mathcal{T}$ and $\mathcal{M}$, respectively. Thus, for arc-length coordinate $s(s_0)$ and stress-free reference coordinate s_0, the membrane tension τ and bending moment b are

$$\tau = \mathcal{T}\left(\frac{ds}{ds_0} - 1\right), \quad b = \mathcal{M}\kappa, \tag{2}$$
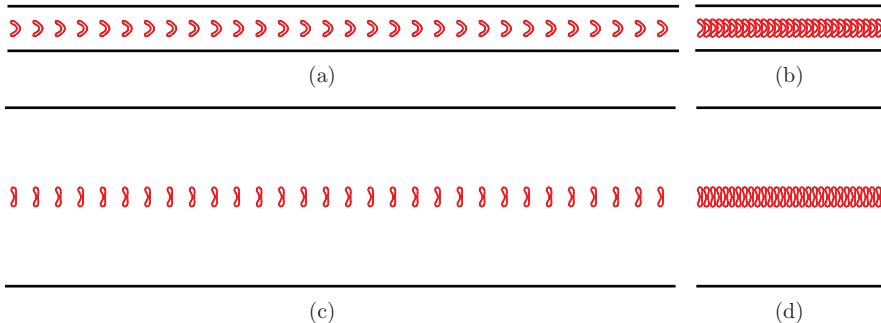
FIG. 3. Base configurations: (a) $\phi = 0.2$ and $W = 10r_0$, (b) $\phi = 0.7$ and $W = 10r_0$, (c) $\phi = 0.2$ and $W = 40r_0$, and (d) $\phi = 0.7$ and $W = 40r_0$.

where κ is the curvature. Though these are linear relations, we emphasize that the net traction on the fluid due to the capsule membranes includes all geometric nonlinearity as

$$\Delta\boldsymbol{\sigma} = \frac{\partial \mathbf{t}\tau}{\partial s} + \frac{\partial}{\partial s}\left(\frac{\partial b}{\partial s}\mathbf{n}\right), \tag{3}$$

where $\mathbf{t}$ is the membrane unit tangent and $\mathbf{n}$ is its outward directed unit normal. We note that this specific model has been used in previous capsule model systems [28,66]. Although it neglects some nonlinear contributions to the full Helfrich strain energy [67], results have confirmed that these terms are unimportant in flows with still more significant strains [66].

Matching the suspending fluid, the fluid within the capsules is also taken to be Newtonian with viscosity μ. Red blood cells are thought to have an elevated cytosol viscosity [68,69], though it has been shown that a matched viscosity model reproduces phenomena in two dimensions [28,66,70] and provides quantitative agreement for the suspension effective viscosity in three dimensions [3,44]. This simplification has reproduced many of the qualitative features of actual red-blood-cell flow in three dimensions, including the Fåhraeus-Lindqvist effect, the margination of larger stiffer capsules, the blunted mean velocity profile, and the nonmonotonic dependence of the effective viscosity on vessel size [44,71].

The relative flexibility of the capsules is quantified with a capillary-number-like parameter

$$\mathrm{Ca} \equiv \frac{\mu U r_0^2}{\mathcal{M}}, \tag{4}$$

which can be interpreted as the ratio of a capsule relaxation time to advection time. For most results, we take $\mathrm{Ca} = 15.2$; the relative importance of flexibility this parametrizes is investigated in Sec. VII. The tension modulus is relatively large compared to the bending modulus

$$\frac{r_0^2 \mathcal{T}}{\mathcal{M}} = 50, \tag{5}$$

which provides a large tensile stiffness to model the near incompressibility of many capsule membranes. Baseline configurations are obtained by simulating the flow without perturbations for time $t = 5r_0\mu/\mathcal{T}$, which is sufficient for the capsules to each assume the steady flow-deformed geometries shown in Fig. 3.

III. NUMERICAL METHODS

The Reynolds numbers of cell-scale blood flow, or similar capsule suspensions in microfluidic devices, are small $\mathrm{Re} \lesssim 0.01$ [3], so inertia is neglected in the present study, which enables a boundary integral formulation of the flow equations [72,73]. To evaluate velocities, we use the same particle-mesh-Ewald algorithm generalized for Stokes flow [74] as used in previous studies [28,66]. It is built upon periodic-space Green's functions [75], with the no-slip condition at the channel walls

enforced via a penalty method [28]. Consistent with the neglect of fluid inertia, the mass of the capsule membranes is likewise neglected. As such, the membrane position $\mathbf{x}(t)$ is simply advected as [3]

$$\frac{d\mathbf{x}}{dt} = \mathbf{u}[\mathbf{x}(t)], \qquad (6)$$

where $\mathbf{u}(\mathbf{x})$ is the local velocity calculated from the boundary integral equation. The time dependence of $\mathbf{u}$ comes only through the membrane geometry $\mathbf{x}(t)$. Although the constitutive model and viscous flow equations are themselves linear, in considering (6) it is important to recognize that $\mathbf{u}(\mathbf{x})$ still includes nonlinearities associated with the geometric factors contributing to the surface tractions (3). These expressions are evaluated numerically using Fourier methods [28], with each capsule discretized by $n = 25$ collocation points except when noted. The full list of $M = nN$ total collocation points is represented by the notation $\vec{\mathbf{x}} \equiv \{x_1^{(1)}, x_2^{(1)}, \ldots, x_2^{(M)}\}$. Nonlinear operations are computed with four times this amount to counter aliasing errors [3,11]. A second-order Runge-Kutta scheme is used to integrate (6) in time, which is crafted for the collocation points as

$$\frac{d\vec{\mathbf{x}}}{dt} = \vec{\mathbf{u}}(\vec{\mathbf{x}}) \quad \text{or equivalently} \quad \frac{dx_i^{(\alpha)}}{dt} = u_i^{(\alpha)}(\vec{\mathbf{x}}) \quad \text{for } i = 1,2; \; \alpha = 1, \ldots, M, \qquad (7)$$

with time step $\Delta t = 0.001 \mu r_0 / \mathcal{T}$.

As they evolve and interact, capsules can come into near contact. Although the boundary integral formulation is unrestricted in this regard by any underlying volume (area) filling mesh discretization, accumulation of even small numerical errors can lead to erroneous interactions between nearby capsules, particularly if the intercapsule spacing becomes comparable to the capsule surface collocation point spacing. In the long DNSs of subsequent behavior, this is countered by introducing a regularizing short-range repulsion between membrane collocation points. We employ the same formulation as past efforts [28,66], with forces zero beyond the distance $0.2r_0$. However, this force is not part of the stability analysis, so the principal results of this study are wholly independent of it.

Similarly, in the course of long simulations the area of the capsules can also change via the accumulation of small numerical errors, though this happens slowly since the area is a low-order moment of the capsule shape and therefore well resolved. Still, a weak variational correction is used to preserve constant capsule areas indefinitely [28]. This also is only included for the DNSs, so the stability results are likewise independent of it.

IV. STABILITY ANALYSIS FORMULATION

A. Measure of configurational stability

Since our goal is to describe the geometric disruption of capsule trains, the measure describing the growth of instabilities is based on the membrane displacement from its unperturbed uniformly advecting baseline configuration. For perturbations applied at time $t = 0$, this is

$$\boldsymbol{\varepsilon}(t) = \mathbf{x}(t) - \mathbf{x}_b(t), \qquad (8)$$

where $\mathbf{x}_b(t)$ represents the corresponding unperturbed case described in Sec. II. The overall disturbance amplitude is quantified by

$$\|\boldsymbol{\varepsilon}\| = \int_{\text{all } C} (\boldsymbol{\varepsilon} \cdot \boldsymbol{\varepsilon})^{1/2} dl, \qquad (9)$$

where C are the capsule membranes. This measure is not unique and no unique measure is expected to exist for so complex a system [47], though it is appropriate for our objectives since $\mathbf{x}$ fully describes the system state and $\boldsymbol{\varepsilon}$ directly describes the geometric disruption we study. In essence, it matches the corresponding metrics used previously for the stability of settling spheres [50,52]. This measure obviously does not correspond to a mechanical energy, as is available for finite-Reynolds-number incompressible fluid flow and thus lacks the additional conservation properties such an energy-based

measure would embody. The capsules do store strain energy, but any measure that includes it would also introduce an additional challenge in that strain energy is invariant to capsule translation or rigid-body rotation. Such constant-energy perturbations, which we anticipate might be hydrodynamically important for seeding instabilities (and indeed are in cases), do not correspondingly perturb the strain energy. Thus, we do need to be mindful that equal $\|\boldsymbol{\varepsilon}\|$ disturbances do not necessarily correspond to equal mechanical energies. This is revisited in Sec. VII, where the elastic energies corresponding to most amplifying perturbations are considered.

B. Linearization

Since $\vec{\mathbf{u}}(\vec{\mathbf{x}})$ couples all the capsule and wall collocation points, which therefore includes significant nonlinearity due to geometric factors, direct linearization of (7) is challenging. However, it is straightforward and equally effective to construct a corresponding linearized system through numerical evaluation of $\mathbf{u}(\mathbf{x})$ in Eq. (7). Expanding (7) for small positional perturbation $\vec{\boldsymbol{\delta}}$ yields

$$\frac{\partial(\vec{\mathbf{x}} + \vec{\boldsymbol{\delta}})}{\partial t} = \vec{\mathbf{u}}(\vec{\mathbf{x}} + \vec{\boldsymbol{\delta}}) = \frac{\partial \vec{\mathbf{x}}}{\partial t} + \mathbf{A}(\vec{\mathbf{x}})\vec{\boldsymbol{\delta}} + \mathcal{O}(\|\vec{\boldsymbol{\delta}}\|^2), \tag{10}$$

where $\mathbf{A}$ thus includes the first-order coupling for the present $\vec{\mathbf{x}}$ configuration due to perturbation $\vec{\boldsymbol{\delta}}$. In practice, this is constructed by systematically perturbing the system and evaluating the velocity. Specifically, each column of $\mathbf{A}$ is calculated by perturbing one of the collocation points $\alpha \in \{1, \ldots, M\}$ in one of the coordinate directions $i \in \{1,2\}$ and calculating $\vec{\mathbf{u}}(\vec{\mathbf{x}} + \vec{\boldsymbol{\delta}})$. Since only the (i,α) component of the $2M$-length vector list $\vec{\boldsymbol{\delta}}$ in Eq. (10) is perturbed (by δ),

$$\delta_j^{(\beta)} = \begin{cases} \delta & \text{for } j = i, \ \beta = \alpha \\ 0 & \text{otherwise,} \end{cases} \tag{11}$$

which provides the i-α column of $\mathbf{A}$ as

$$A_{ij}^{(\alpha\beta)} = \frac{u_j^{(\beta)}(\vec{\mathbf{x}} + \vec{\boldsymbol{\delta}}) - u_j^{(\beta)}(\vec{\mathbf{x}})}{\delta} \quad \text{for } j = 1,2; \ \beta = 1, \ldots, M. \tag{12}$$

Repeating this for all collocation points and both coordinate directions yields all columns of $\mathbf{A}$. The translation of the baseline train of capsules due to the mean flow is common to the perturbed and unperturbed $\vec{\mathbf{u}}$ in Eq. (12), so it does not contribute to $\mathbf{A}$. It is confirmed that results are independent of the $\delta = 10^{-5} r_0$ used here.

Generating the full $2M \times 2M$ matrix $\mathbf{A}$ in this way requires about the same computational effort as $2M$ numerical time steps of the flow solver and would be prohibitive in many numerical flow solutions. For the particular configurations we consider, periodicity of the domain and the identical character of all the capsules can be exploited to reduce this to $2M/N$. An advantage of the boundary integral discretization is that only the surfaces of the capsules are discretized, so this is not an insurmountable calculation. The use of high-resolution Fourier methods further reduces the number of points necessary to accurately represent the membranes and thus describe the stability through $\mathbf{A}$. The largest case presented here has $2M = 10^5$, which is comparable to the number of time steps of a typical direct numerical simulation of this system.

With $\mathbf{A}$, the evolution of any sufficiently small perturbation $\vec{\boldsymbol{\varepsilon}}$ is governed by the linear system

$$\frac{\partial \vec{\boldsymbol{\varepsilon}}}{\partial t} = \mathbf{A}\vec{\boldsymbol{\varepsilon}}, \tag{13}$$

with the matrix-exponential solution

$$\vec{\boldsymbol{\varepsilon}}(t) = \vec{\boldsymbol{\varepsilon}}_0 \exp \mathbf{A}t \tag{14}$$

for the initial condition $\vec{\boldsymbol{\varepsilon}}(0) = \vec{\boldsymbol{\varepsilon}}_0$. The $\exp \mathbf{A}t$ factor thus describes its temporal behavior.
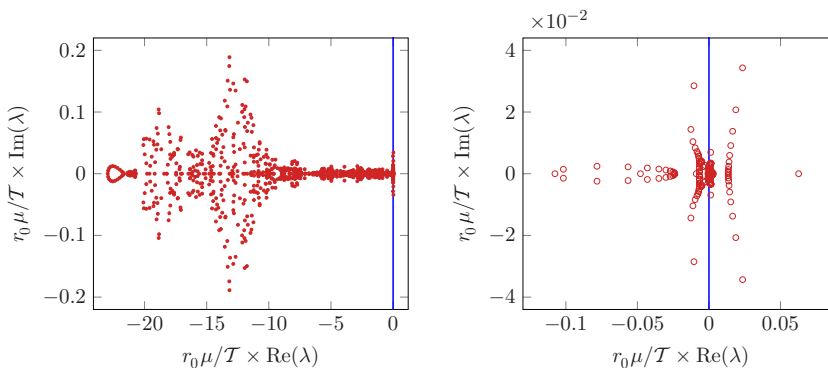
FIG. 4. Eigenvalues of $\mathbf{A}$ for $W = 40r_0$ and $\phi = 0.7$ with $N = 20$ capsules.

C. Eigensystem

The matrix $\mathbf{A}$ is real and nonnormal ($\mathbf{A}\mathbf{A}^{\mathrm{T}} \neq \mathbf{A}^{\mathrm{T}}\mathbf{A}$), as can be anticipated by the character of the vector Green's function of the Stokes operator, so in general it will not have a full set of orthogonal eigenvectors. Eigenvalues for a typical configuration are shown in Fig. 4. Nearly all of their real components are negative, as expected for a predominantly viscous system, though 75 of the 1000 total in this example do have positive real components, indicating asymptotic instability. The most amplifying is real valued and corresponds to a tilting perturbation, which we analyze subsequently.

Though it is not diagonalizable, the eigensystem of $\mathbf{A}$ does dictate the $t \to \infty$ behavior of small perturbations, so long as they do not trigger significant nonlinear interactions before this behavior is realized [46]. Here we consider its behavior for this reason, in addition to using it as a point of reference with respect to predicted transient growth, which we consider in the following subsection. With $\vec{\lambda}(\mathbf{A})$ representing the $2M$ eigenvalues of $\mathbf{A}$, the nominal spectral abscissa of the system is its most-amplifying component

$$\alpha \equiv \max\{\mathrm{Re}[\vec{\lambda}(\mathbf{A})]\}. \tag{15}$$

The corresponding most-amplified eigenvalue and its associated eigenvector are defined as λ_α and $\vec{\mathbf{s}}_\alpha$, respectively. For $t \to \infty$, an initial perturbation $\boldsymbol{\varepsilon}(0) = \hat{\varepsilon}\mathbf{s}_\alpha$ will evolve as

$$\boldsymbol{\varepsilon}(t) = \hat{\varepsilon}\mathbf{s}_\alpha \exp \lambda_\alpha t. \tag{16}$$

D. Nonmodal analysis

Following a common reasoning [47,76], a $t \to 0^+$ amplification bound is defined by the numerical abscissa

$$\eta \equiv \max\left\{\mathrm{Re}\left[\vec{\lambda}\left(\frac{\mathbf{A} + \mathbf{A}^{\mathrm{T}}}{2}\right)\right]\right\}, \tag{17}$$

which recovers $\eta = \alpha$ for normal $\mathbf{A}$. This is the maximum initial amplification of any perturbation, though this growth rate will not necessarily persist.

In addition to the short-time growth rate, of particular interest is the form of the most-amplifying perturbation and the most dangerous growth at later times. This is determined from a singular-value decomposition

$$\exp \mathbf{A} t = \mathbf{U}\boldsymbol{\Sigma}\mathbf{V}^{\mathrm{T}}, \tag{18}$$

where the ordered singular values $\vec{\sigma}(t)$ form the diagonal matrix $\boldsymbol{\Sigma}$, and $\mathbf{U}$ and $\mathbf{V}$ are matrices constructed of orthonormal left and right singular vectors, respectively. Though non-normality
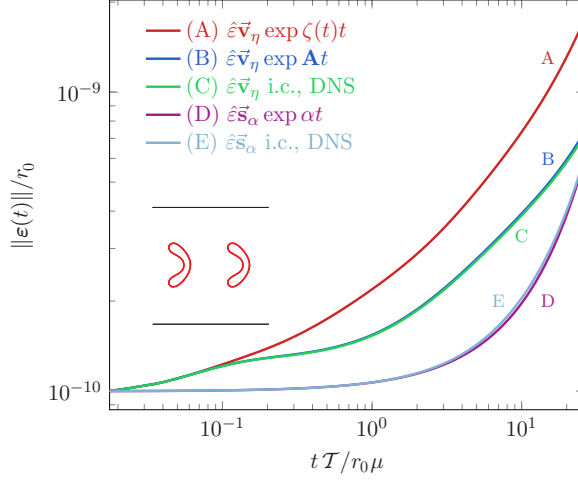
FIG. 5. Perturbation amplification in time: curve A, transient growth based on maximum time-dependent amplification $\zeta(t)$ from (20) for initial perturbation $\hat{\varepsilon}\vec{\mathbf{v}}_\eta$; curve B, direct evaluation of the matrix exponential $\exp \mathbf{A}t$ from (14) for $\hat{\varepsilon}\vec{\mathbf{v}}_\eta$, which matches curve C from the corresponding DNS; and curve D, $\exp \alpha t$ for $\hat{\varepsilon}\vec{\mathbf{s}}_\alpha$ from (16), which matches the large t behavior of curve E from the corresponding DNS.

couples the linear disturbances, their maximum time-dependent evolution can be tracked by reevaluating (18) as a function of time,

$$G(t) \equiv \| \exp \mathbf{A}t \| = \max_{j,\beta} \sigma_j^{(\beta)}(t). \tag{19}$$

The corresponding instantaneous maximum growth rate is then

$$\zeta(t) \equiv \frac{d \ln G(t)}{dt}. \tag{20}$$

For $t \to \infty$ this should converge to the eigenvalue associated with the least stable eigenvalue $\zeta \to \alpha$ and for $t \to 0^+$ it converges to the maximum transient amplification $\zeta \to \eta$. If $\zeta(t) > \alpha$ for any range of t, transient growth can outpace asymptotic eigensystem growth in that range.

E. Character and verification of the linear system

The construction of $\mathbf{A}$ and its analysis is intricate, so it is important to verify that it indeed represents a linearization of the full system. This also serves to introduce the basic behavior we will see in most of the results. For verification, linear predictions based on $\mathbf{A}$ are compared with full DNS calculations for small perturbations. For $\phi = 0.2$ and $W = 10r_0$, we compare the predicted growth of $\|\vec{\varepsilon}\|$ for $\hat{\varepsilon} = 10^{-10}r_0$ perturbations against the DNS for different initial conditions. Before nonlinear effects manifest, which is avoided with $\hat{\varepsilon}$ so small, agreement should be limited only by the accumulation of numerical approximation errors. For numerical evaluation, $\|\vec{\varepsilon}\|$ from (9) is approximated as

$$\|\vec{\boldsymbol{\varepsilon}}\| = \frac{1}{M} \sum_{i=1}^{M} \sqrt{\left[\varepsilon_x^{(i)}\right]^2 + \left[\varepsilon_y^{(i)}\right]^2}. \tag{21}$$

Two main verification comparisons are made in Fig. 5. For the initial perturbation $\hat{\varepsilon}\vec{\mathbf{v}}_\eta$, the predicted cumulative amplification based on $\| \exp \mathbf{A}t \|$ is compared with the corresponding DNS and shown to agree (curves B and C). We also see that both match the $t \to 0^+$ prediction based upon $\zeta(t \to 0)$ and that for $t > 0$ they are indeed bounded by this. The second comparison is for

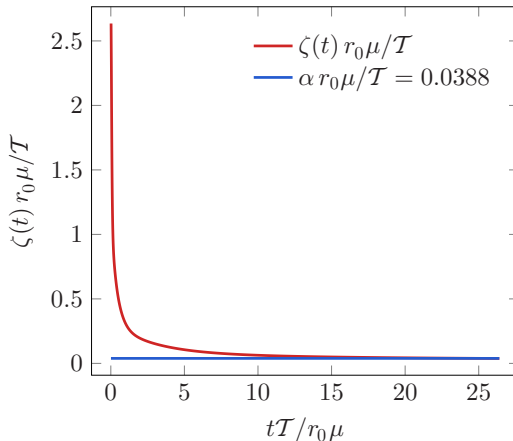FIG. 6. Evolving maximum growth rate $\zeta(t)$ analyzed in Fig. 5.

the $t \to \infty$ behavior, based on α for the initial condition $\hat{\varepsilon}\vec{\mathbf{s}}_\alpha$ and a corresponding DNS. These also agree (curves D and E in the figure) in that they overlap at long times, with a relative amplification difference less than 5% at $t = 10r_0\mu/\mathcal{T}$ and less than 2% at $t = 100r_0\mu/\mathcal{T}$. Note that their good agreement at all times, not just for $t \to \infty$, indicates that in this case $\vec{\mathbf{s}}_\alpha$ itself is not strongly coupled with other linear disturbances.

In Fig. 6 we see that at short times $\zeta(t)$ significantly exceeds α, confirming the small-t behavior of Fig. 5. At later times, we likewise confirm that $\zeta \to \alpha$, as it should. Despite the long-time behavior, we anticipate that for finite perturbations, the rapid transient growth might be a significant mechanism leading to nonlinear saturation and subsequent disruption of the capsule train. This is considered in Sec. VI. In the following section we examine the character of the most-amplifying disturbances.

V. STABILITY RESULTS

We consider transient amplification in Sec. V A and long-time asymptotic amplification in Sec. V B for the four base flows visualized Fig. 3. Additional configurations are introduced in Sec. V C to map the boundaries between different disturbance-form regimes. The narrow channels of these configurations are insufficient to preserve the regularity of the capsule trains, so for comparison we also introduce a very narrow channel with $W = 4r_0$ in Sec. V D. In this case, the capsule train persists, seemingly indefinitely, and we characterize its apparent stability.

A. Transient amplification

Figure 7 shows the initial transient amplifications η from (17). In all four cases, η depends, at least weakly, upon the channel length, with an apparent asymptotic long-L power-law behavior for sufficiently large L. For all cases, the power laws provide good fits for $N \gtrsim 20$ capsules, suggesting that in this limit the discrete character of the capsules *per se* becomes relatively unimportant, as might be expected for 20 capsules per wavelength of the disturbances. An implication is that an effective medium model and continuous dispersion relation might afford a reasonable description of the response, though we do not pursue this here. The apparent noninteger power laws in Fig. 7 suggests the existence of an anomalous dimension [77], though its specific form has not been found.

For both ϕ and larger L, the narrow channels are significantly more amplifying. However, this behavior is different in shorter channels. For small L, the proximity of the walls appears to be less important and we see about a factor of 5 more significant transient amplification for the more densely packed channels, irrespective of width, suggesting that capsule-capsule interactions themselves are
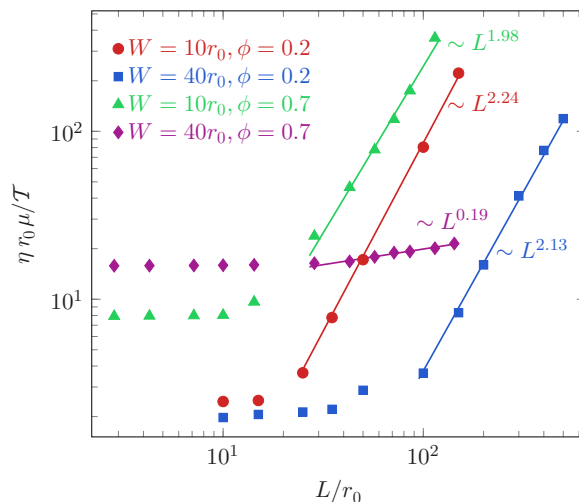
FIG. 7. Numerical abscissa η from (17) for different lengths L for the channels of Fig. 3. The straight lines are power-law fits.

most important in this limit. Still, the amplification rates for shorter channels are much smaller than those in most of the longer channels.

With such different behavior in the amplification rates, it is not surprising that the corresponding $t \to 0^+$ most-amplifying disturbances visualized in Fig. 8 show diverse structures. The $\phi = 0.2$ wide-channel case visualized in Fig. 8(b) shows a longitudinal displacement wave, with each
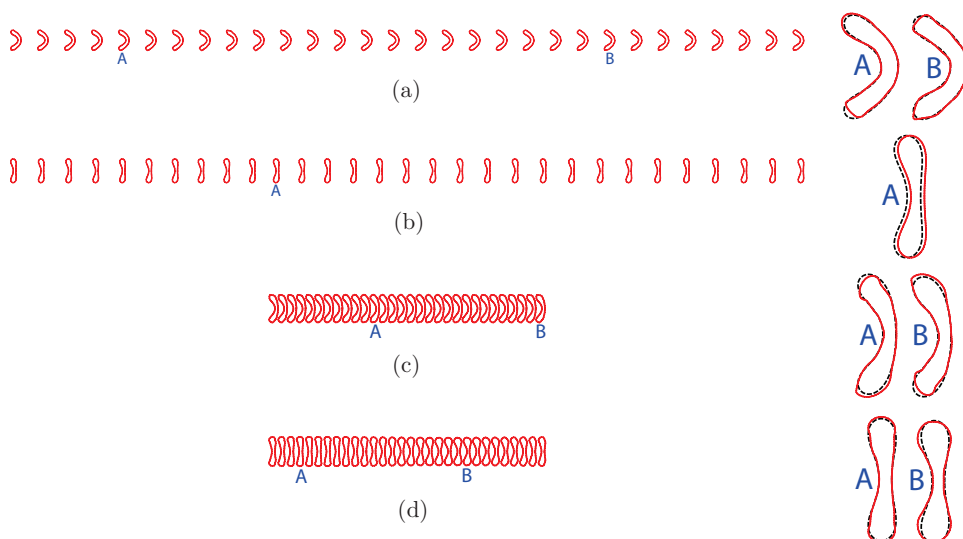

FIG. 8. Most transiently amplifying (nonmodal) disturbances for the baseline cases with $N = 30$ of Fig. 3: baseline $\vec{\mathbf{x}}$ (dashed line) and perturbations visualized as $\vec{\mathbf{x}} + a\hat{\varepsilon}\vec{\mathbf{v}}_\eta$ (solid line) with $a\hat{\varepsilon} = 3.5$: (a) $\phi = 0.2$ and $W = 10r_0$, asymmetric deformation; (b) $\phi = 0.2$ and $W = 40r_0$, longitudinal translation; (c) $\phi = 0.7$ and $W = 10r_0$, asymmetric deformation; and (d) $\phi = 0.7$ and $W = 40r_0$, symmetric deformation. These relatively large amplitudes aid visualization, though some of the features appear exceptionally sharp due to geometric nonlinearity. The A and B labels indicate the specific magnified capsules.

capsule displaced in the streamwise direction without an obvious change of shape. As such, the overall disturbance appears as a compression-expansion wave of the capsule spacing. The other disturbances visualized in Figs. 8(a), 8(c), and 8(d) appear primarily as distortions of individual capsules; although consistent with the L dependences of Fig. 7, these also manifest as wavelike perturbations correlated across all the capsules. They are asymmetric for the narrow channels in Figs. 8(a) and 8(c) and symmetric in Fig. 8(d). Similar long-wavelength disturbances are most amplifying for capillary instability of low-Reynolds-number core-annular flows [78,79], though we do not pursue any possible correspondence to this configuration herein. We note that such disturbances that distort individual capsules are hard to visualize. For genuinely small $\hat{\varepsilon}$, for which the linear approximation is quantitatively accurate, they would be imperceptible if plotted as $\vec{\mathbf{x}} + \hat{\varepsilon}\vec{\mathbf{v}}_\eta$. For visualization, they are therefore artificially increased by a factor a as $\vec{\mathbf{x}} + a\hat{\varepsilon}\vec{\mathbf{v}}_\eta$, which makes them visible but unfortunately also distorts their shapes, which leads to a kinky appearance due to geometric nonlinearities. These visualizations should be construed as showing the approximate direction and relative amplitude of the membrane perturbation, not strictly the membrane shape.

Motivated by these visualizations, we quantify the disturbances with low-order moments of each capsule shape C. These are selected to emphasize their main apparent characteristics:

$$x_c = \frac{1}{l_0} \int_C \varepsilon_x dl, \tag{22}$$

$$y_c = \frac{1}{l_0} \int_C \varepsilon_y dl, \tag{23}$$

$$M_x = \frac{1}{l_0 r_0^2} \int_C \varepsilon_x^3 dl, \tag{24}$$

$$M_y = \frac{1}{l_0 r_0^2} \int_C \varepsilon_y^3 dl, \tag{25}$$

$$M_{xy} = \frac{1}{l_0 r_0} \int_C \varepsilon_x \varepsilon_y dl, \tag{26}$$

where x is the streamwise and y is the cross-stream coordinate, as labeled in Fig. 2. Third-order rather than second-order moments are used for M_x and M_y to preserve the sign of the perturbation. The relative values of (22)–(26) are plotted for all capsules in Fig. 9. These confirm the predominance of particular moment contributions for the different cases, as might be anticipated from the visualizations. Their wavelike character again suggests that a continuum model might afford a natural way to analyze the behavior of the dominant transient disturbance (and its asymptotic analog; see Fig. 12) if an effective material model or averaging procedure could be deduced. This is not attempted here.

B. Asymptotic amplification

The maximum asymptotic amplification rates α, corresponding to the same four cases of Fig. 3, are shown in Fig. 10. These growth rates are all slower than the corresponding η, typically by over a factor of 10. Again, for sufficiently long L, the more-narrow channels also show length dependence, though with different powers than for η. However, the wider channels do not, at least for up to the 100 capsules considered. This is true even when the channel length is many times its width. The more-narrow $W = 10r_0$ channels are most amplifying for all L. For $\phi = 0.2$, its L dependence is similar to the transient behavior $\eta \sim L^2$, though for $\phi = 0.7$ it is less sensitive to L, with $\alpha \sim L^{3/4}$ rather than matching $\eta \sim L^2$.

Given these diverse asymptotic amplification rates, we again anticipate different characters for the corresponding disturbances visualized in Fig. 11. Both wide channels [Figs. 11(b) and 11(d)] show a predominantly tilting disturbance, in which all the capsules collectively tilt. The uniformity of this tilt rate is confirmed to be M_{xy} dominant in Figs. 12(b) and 12(d). Their lack of a streamwise wavelike structure (constant M_{xy}) is consistent with the $\alpha \sim L^0$ behavior seen for both these cases. In
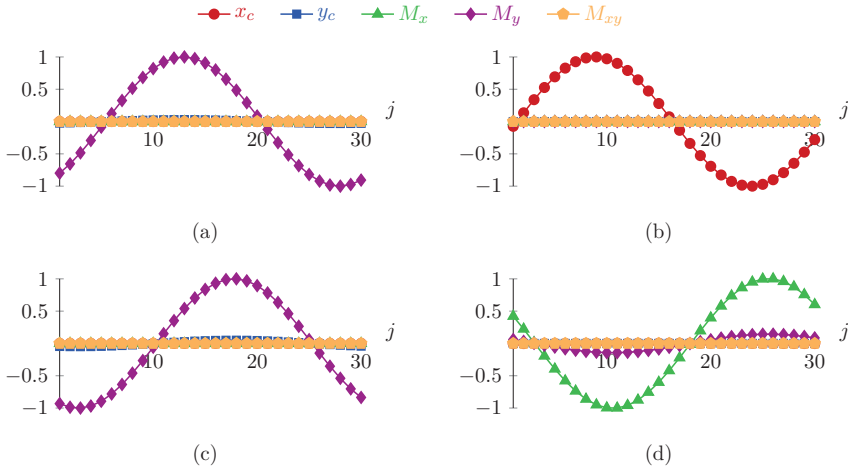
FIG. 9. Disturbance metrics (22)–(26) for all $j = 1, \ldots, N$ capsules for $N = 30$ applied to the most amplifying transient disturbances visualized in Fig. 8: (a) $\phi = 0.2$ and $W = 10r_0$, (b) $\phi = 0.2$ and $W = 40r_0$, (c) $\phi = 0.7$ and $W = 10r_0$, and (d) $\phi = 0.7$ and $W = 40r_0$. All metrics are plotted for all cases, normalized by the largest value of any.

contrast, both narrow-channel configurations show a wavelike transverse displacement, also different from the corresponding most-amplifying transient disturbances though still sinuous. These are M_y dominant, as shown in Figs. 12(a) and 12(c).

C. Disturbance regime boundaries

The diverse transiently and asymptotically most amplifying disturbances shown in Figs. 8 and 11 suggest a more complete mapping of the configuration parameters to identify boundaries between these regimes. These are illustrated in Fig. 13 for ranges of ϕ and W, where the nominal disturbance character is based on the maximum values of the (22)–(26) metrics. Only the nonuniform tilt in Fig. 13(b) was not directly observed in our four focus cases. It shows an obvious L-periodic wavelike variation from the uniform tilt shown in Figs. 11(b) and 11(d).
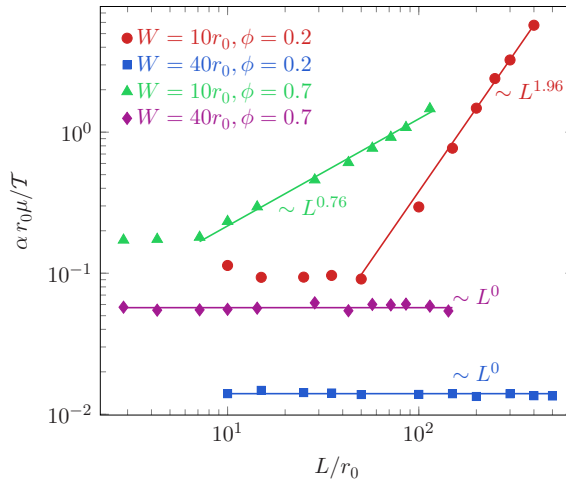

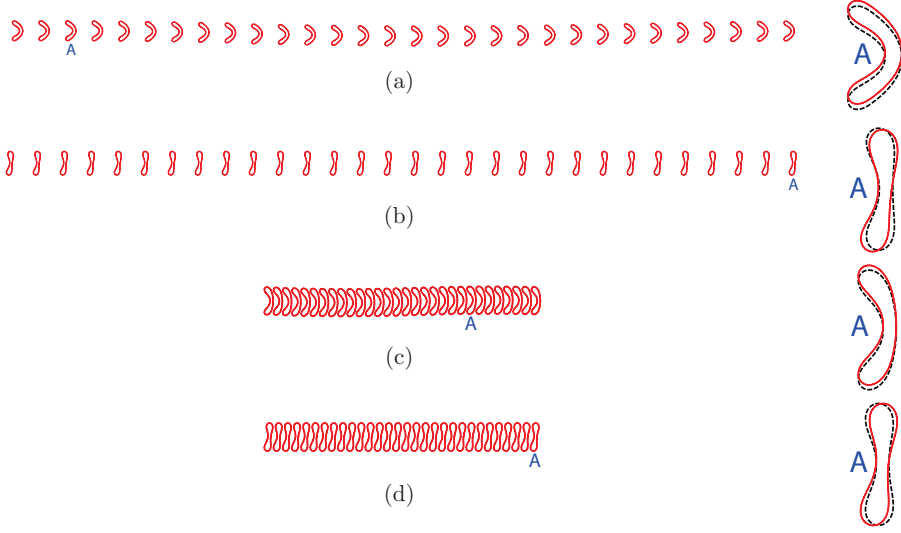FIG. 10. Spectral abscissa α from (15) for different for cases of Fig. 3. The straight lines are power-law fits.

FIG. 11. Most asymptotically ($t \to \infty$) amplifying modal disturbances for the baseline case with $N = 30$ visualized in Fig. 3: baseline $\vec{\mathbf{x}}$ (dashed line) and perturbations visualized as $\vec{\mathbf{x}} + a\hat{\varepsilon}\vec{\mathbf{s}}_\alpha$ (solid line) with $a\hat{\varepsilon} = 3.5$: (a) $\phi = 0.2$ and $W = 10r_0$, transverse translation; (b) $\phi = 0.2$ and $W = 40r_0$, uniform tilt; (c) $\phi = 0.7$ and $W = 10r_0$, transverse translation; and (d) $\phi = 0.7$ and $W = 40r_0$, uniform tilt. The selected magnified capsules are labeled accordingly.

D. An empirically stable, narrow-channel configuration

Figure 14 shows that in this case the capsules bend into a two-dimensional analog of the bulletlike shapes seen in blood cells and empirical observations from long-time DNSs suggest indefinite persistence of this single-file flow, even when perturbed. (In this case $n = 35$ was used to resolve the more significant capsule deformations.) We analyze this case for comparison. Despite the empirical
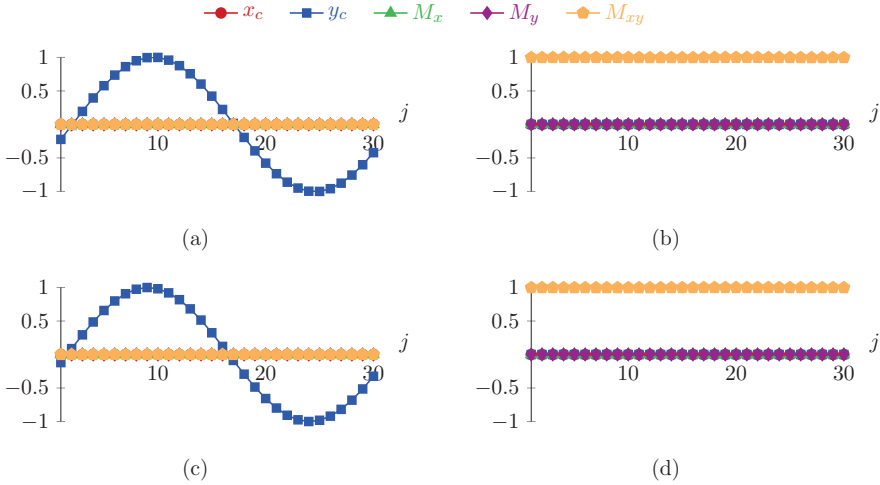

FIG. 12. Disturbance metrics (22)–(26) for all $j = 1, \ldots, N$ capsules for $N = 30$ applied to the most amplifying transient disturbances visualized in Fig. 11: (a) $\phi = 0.2$ and $W = 10r_0$, (b) $\phi = 0.2$ and $W = 40r_0$, (c) $\phi = 0.7$ and $W = 10r_0$, and (d) $\phi = 0.7$ and $W = 40r_0$. All metrics are plotted for all cases, normalized by the largest value of any.
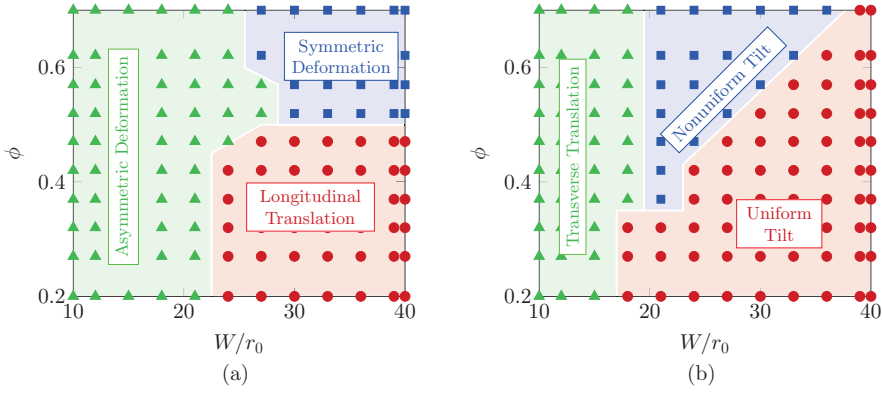
FIG. 13. Character of the most amplifying disturbances for a range of channel widths and packing fractions: (a) transient $\vec{\mathbf{v}}_\eta$ disturbances and (b) asymptotic $\vec{\mathbf{s}}_\alpha$ disturbances.

stability, linear analysis suggests both transient amplification ($\eta = 0.28$) and asymptotic instability ($\alpha = 0.0018$), though these are at least seven times smaller than those seen for the wider channels (Figs. 7 and 10). Similar to wider channels, the corresponding $\vec{\mathbf{v}}_\eta$ show asymmetric distortion reflected by M_y [Figs. 14(b) and 14(d)], whereas the $\vec{\mathbf{s}}_\alpha$ shows a capsule-to-capsule varying mix of tilt and asymmetric distortion, which is strongest for a particular capsule [$j = 7$ in Figs. 14(c) and 14(e)].

The amplifications of different disturbances are shown in Fig. 15. While DNSs initialized with $\hat{\varepsilon}\vec{\mathbf{v}}_\eta$ and $\hat{\varepsilon}\vec{\mathbf{s}}_\alpha$ do indeed initially reflect the predicted linear growth, as they must, it does not persist, presumably due to nonlinear effects. The upper-bound $\zeta(t)$ growth is not realized and the $\vec{\mathbf{s}}_\alpha$ disturbance likewise saturates also due to nonlinear effects associated with tight confinement. The approximately constant $\|\vec{\boldsymbol{\varepsilon}}\|$ reached in this case at long times is consistent with a persistent tilt of
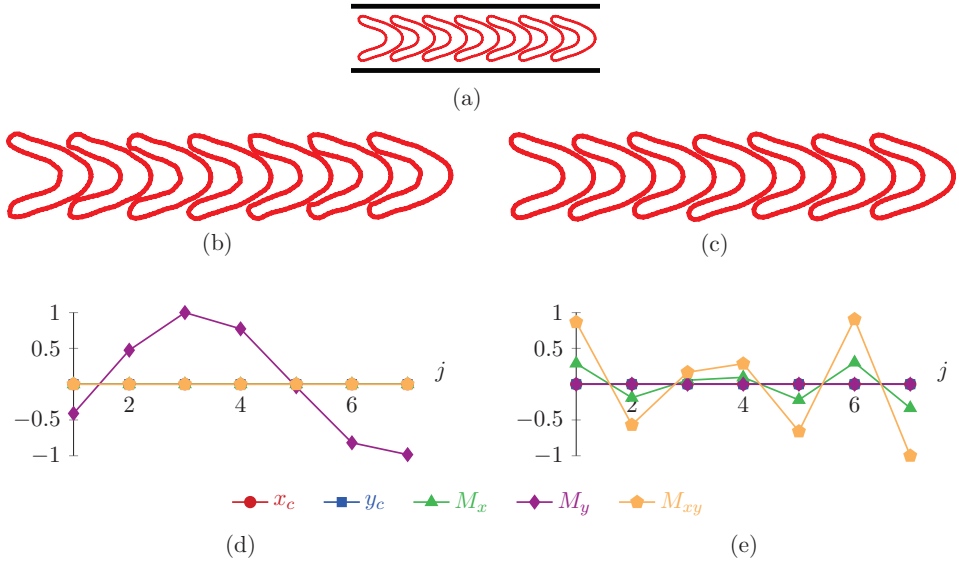
FIG. 14. (a) Baseline configuration for an empirically stable case with $W = 4r_0$, $\phi = 0.5$, and $N = 7$. (b) The $t \rightarrow 0^+$ most amplified transient disturbances $\vec{\mathbf{x}} + 3.5\vec{\mathbf{v}}_\eta$ and (c) the asymptotically most amplified disturbances $\vec{\mathbf{x}} + 3.5\vec{\mathbf{s}}_\alpha$. Also shown are the corresponding disturbance metrics (22)–(26) for (d) $\vec{\mathbf{v}}_\eta$ and (e) $\vec{\mathbf{s}}_\alpha$. The exaggerated displacements cause these to look unphysical, as discussed in Sec. V A in regard to Fig. 8.
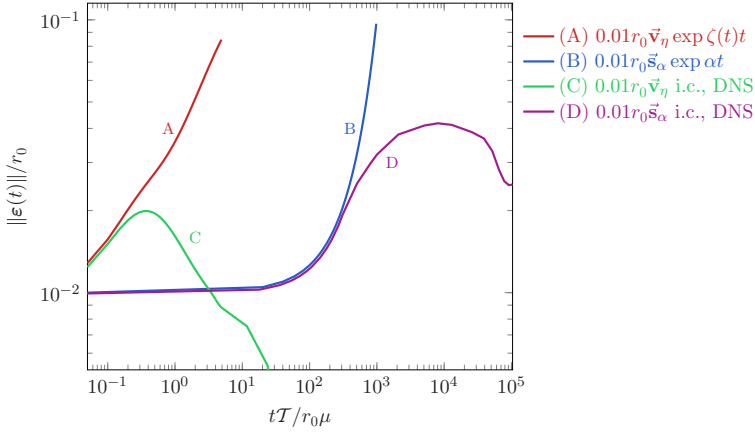
FIG. 15. Disturbance amplification for the empirically stable narrow-channel case, visualized in Fig. 14(a). The DNSs track (curves C and D) the corresponding linear amplifications (curves A and B) only for short times.

the membrane from its initial orientation, though the capsule returns to the same bent shape. Thus, although this case is linearly unstable, significant linear amplification is not realized and might not be expected given the obviously limited range of permissible motions for such tightly confined capsules.

VI. TRANSITION TO DISORDERED FLOW

An important potential consequence of the relatively fast predicted transient growth seen in most cases is that it can significantly reduce time to the onset of significant nonlinear effects. A specific example is shown in Fig. 16 for $\phi = 0.7$ and $W = 40r_0$. The DNS with initial perturbation $\hat{\varepsilon} = 0.001r_0$ (curve D in the figure) shows brief transient growth, but it does not lead directly to obvious nonlinear behavior. Instead, the growth nearly ceases, because only a small portion of $\vec{\varepsilon}$ is associated with the disturbances that are amplified in this transient regime. It is only after $t \gtrsim 1000r_0\mu/\mathcal{T}$ that it again amplifies significantly, and then at a rate consistent with the $t \to \infty$

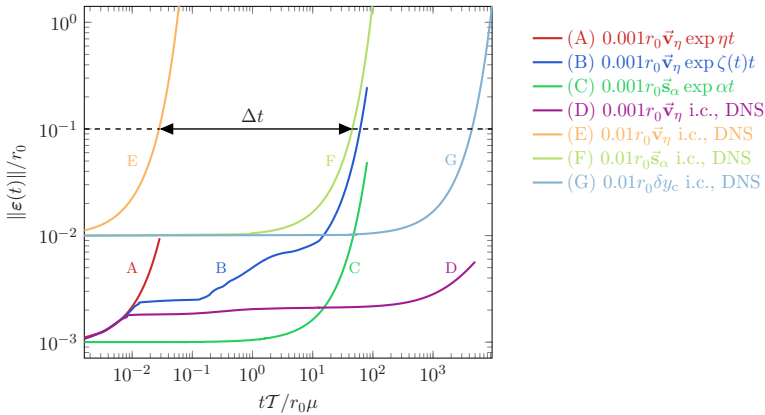FIG. 16. Disturbance amplitude evolution for the wide and dense configuration ($W = 40r_0$ and $\phi = 0.7$) with $\hat{\varepsilon} = 0.001r_0$ and $0.01r_0$ for initial conditions and predictions as labeled. The $\Delta t \approx 10^3 \mathcal{T}/r_0\mu$ labels the approximate difference in time for onset of nonlinear for transient versus eigenvalue estimates for $\hat{\varepsilon} = 0.01r_0$ (see the text).

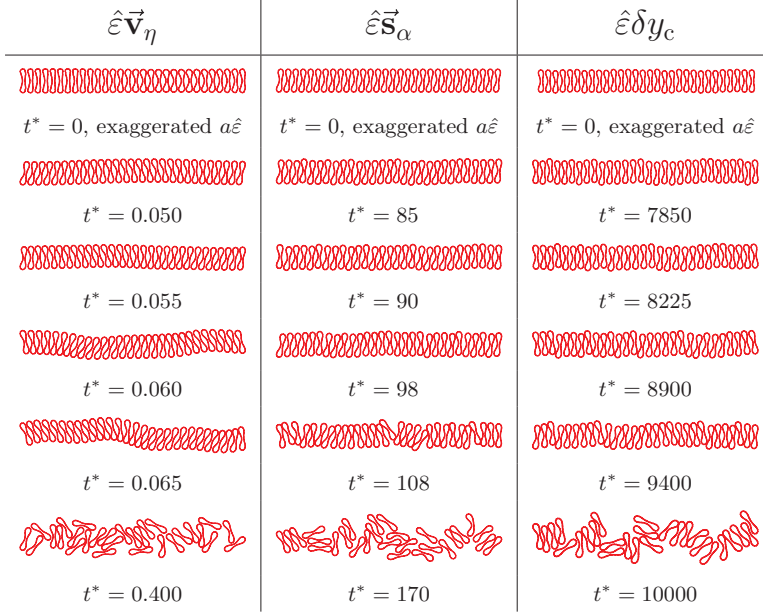| $\hat{\varepsilon}\vec{\mathbf{v}}_\eta$	$\hat{\varepsilon}\vec{\mathbf{s}}_\alpha$	$\hat{\varepsilon}\delta y_{\mathrm{c}}$
$t^* = 0$, exaggerated $a\hat{\varepsilon}$	$t^* = 0$, exaggerated $a\hat{\varepsilon}$	$t^* = 0$, exaggerated $a\hat{\varepsilon}$
$t^* = 0.050$	$t^* = 85$	$t^* = 7850$
$t^* = 0.055$	$t^* = 90$	$t^* = 8225$
$t^* = 0.060$	$t^* = 98$	$t^* = 8900$
$t^* = 0.065$	$t^* = 108$	$t^* = 9400$
$t^* = 0.400$	$t^* = 170$	$t^* = 10000$

FIG. 17. Transition to disordered flow for the $\hat{\varepsilon} = 10^{-2}r_0$ cases of Fig. 16. The exaggeration factor is $a\hat{\varepsilon} = 3.5$ for the initial configuration plot. The walls are not shown; they can be seen for the baseline configuration in Fig. 3(d). The times shown $t^* = t\mathcal{T}/r_0\mu$ were selected to illustrate the development qualitatively.

asymptotic α curve (C). Before this occurs, it remains bounded by the $\zeta(t)$ prediction (curve B). In contrast, for a still small but larger $\hat{\varepsilon} = 0.01r_0$, the initial condition $\hat{\varepsilon}\vec{\mathbf{v}}_\eta$ perturbation leads to nonlinearity much earlier, about 10^3 times faster than would the $t \to \infty$ mechanism for $\vec{\mathbf{s}}_\alpha$, even with the initial condition $\hat{\varepsilon}\vec{\mathbf{s}}_\alpha$. Both the $\hat{\varepsilon}\vec{\mathbf{v}}_\eta$ and $\hat{\varepsilon}\vec{\mathbf{s}}_\alpha$ initial conditions show nonlinear saturation well before a corresponding *ad hoc* perturbation constructed as random $\hat{\varepsilon}\delta y_c$ displacements of the capsule centroids. This *ad hoc* perturbation saturates 100 times more slowly still (curve G).

The subsequent DNS transition to an apparently chaotic flow for $\phi = 0.7$ and $W = 40r_0$ is visualized for three different initial perturbations in Fig. 17. We see that the $\hat{\varepsilon}\vec{\mathbf{v}}_\eta$ initial condition has a different development from the eigenvector $\hat{\varepsilon}\vec{\mathbf{s}}_\alpha$ or *ad hoc* $\hat{\varepsilon}\delta y_c$ disturbances. Its L-scale wavelike structure persists and amplifies before it breaks down into an apparently chaotic flow. The other initial perturbations lead to choppier variations in the capsule train, with shorter features in the streamwise direction. In these cases, the capsule trains seem to first come apart at specific points, before they develop an apparently chaotic behavior, much more slowly than the $\vec{\mathbf{v}}_\eta$ case.

The relatively narrow $W = 10r_0$ with $\phi = 0.2$ [Fig. 3(a)] shows a qualitatively similar amplification for the same three types of initial conditions (Fig. 18), though all of the growth rates are substantially faster, as anticipated based on Figs. 7 and 10. In this case, nonlinear saturation is accelerated only by a factor of 100 for the $\hat{\varepsilon} = 0.01r_0$ initial disturbance $\hat{\varepsilon}\vec{\mathbf{v}}_\eta$ relative to $\hat{\varepsilon}\vec{\mathbf{s}}_\alpha$. The weaker $0.001r_0\vec{\mathbf{v}}_\eta$ perturbation also appears to reach an amplitude consistent with the onset of nonlinear effects within the simulation time shown. The upper-bound $\exp\zeta(t)t$ curve is again consistent with this accelerated saturation.

Unlike the nonlinear breakdown for the densely packed wider channel of Fig. 17, Fig. 19 shows that the three initial conditions in this narrower case have a progression qualitatively similar to a relatively disorganized state. The capsules retain an approximately single-file structure but with the capsules oriented at a range of angles with significant changes of streamwise spacing, as has been observed in similar configurations in both two [80] and three [81] dimensions. Unlike the $W = 40r_0$ and $\phi = 0.7$ case, this configuration does not, at least for the times simulated, show significant
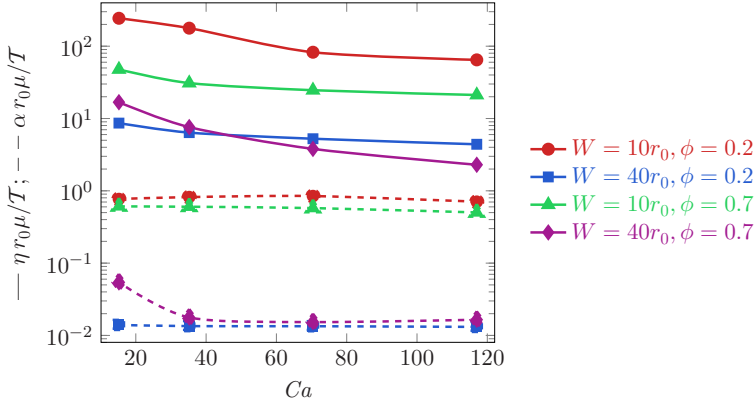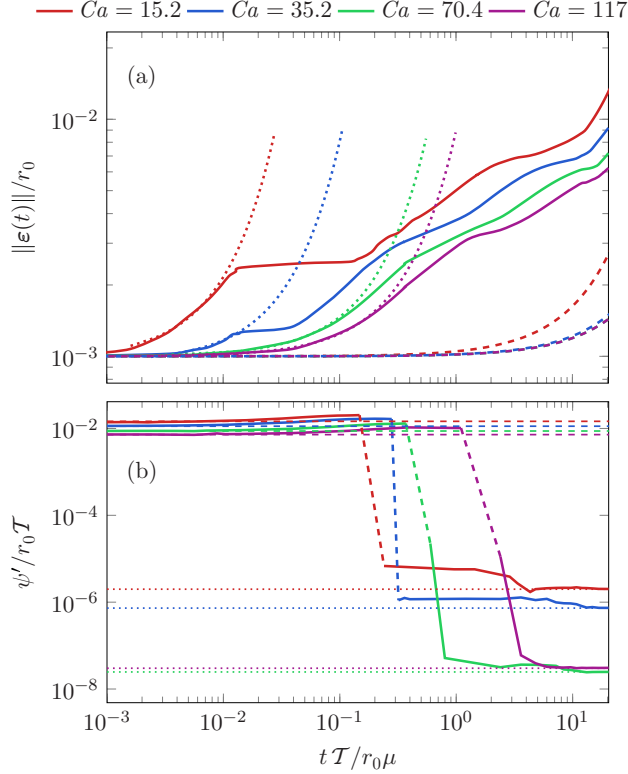
FIG. 18. Disturbance amplitude evolution for the wide and dense configuration ($W = 10r_0$ and $\phi = 0.2$) with $\hat{\varepsilon} = 0.001r_0$ and $0.01r_0$ as labeled. The $\Delta t \approx 10^2 \mathcal{T}/r_0\mu$ labels the approximate difference in time for the onset of nonlinearity for transient versus eigenvalue estimates for $\hat{\varepsilon} = 0.01$ (see the text).

overturning or passing of the capsules, presumably because of some combination of the greater confinement for $W = 10r_0$ and less crowding for $\phi = 0.2$.

VII. ELASTIC STIFFNESS

As discussed in Sec. IV A, the displacement-based measure used to quantify amplification does not have a one-to-one correspondence with a mechanical energy, with the consequence that different perturbations for the same $\|\vec{\boldsymbol{\varepsilon}}\|$ can have different strain energies. We consider this here, and more generally the effect of capsule stiffness, by changing Ca. We consider capsules with up to Ca = 117, starting from the Ca = 15.2 introduced as the basic case in Sec. II, which increases flexibility by decreasing $\mathcal{M}$ by a factor of about 7.7. The tension modulus is adjusted correspondingly per (5).

The consequence of these changes on the initial transient and asymptotic amplification rates is relatively small over this range, as shown in Fig. 20. The asymptotic growth rates are nearly

FIG. 19. Transition to disordered flow for the $\hat{\varepsilon} = 0.01r_0$ cases of Fig. 18. The exaggeration factor is $a\hat{\varepsilon} = 3.5$ for the plot of the initial configuration. The walls are are not shown; they can be seen for the baseline configuration in Fig. 3(a). The times shown $t^* = t\mathcal{T}/r_0\mu$ were selected to demonstrate nonlinear disruption.

FIG. 20. Effect of capsule stiffness on α and η.

FIG. 21. The $W = 40r_0$ and $\phi = 0.7$ case: (a) Predicted disturbance amplitude for different membrane stiffnesses based on η (dotted line), $\zeta(t)$ (solid line), and α (dashed line) and (b) relative strain energy of the transiently most amplified mode $\vec{v}_\zeta(t)$ at time t (solid line). For reference, also shown in (b) are the energies corresponding to $\vec{v}_\eta$ (dotted line) and $\vec{s}_\alpha$ (dashed line). Note that neither plot displays the evolution of the system in time. Rather, they show the maximum possible linear amplification amplitude and corresponding strain energy for an $\hat{\varepsilon} = 0.001r_0$ disturbance at that time. The strain energy can change abruptly as different disturbances become the nominally most dangerous at specific times.

unchanged; only the wide and dense ($W = 40r_0$ and $\phi = 0.7$) case shows a decrease at small $\mathcal{M}$. The transient amplification is more sensitive, as might be expected given that these disturbances generally showed more distortion of the capsule shapes. Still, they only decrease by less than a factor 10, with similar effects on the eventual breakdown. Though we do not simulate smaller or larger Ca because it is computationally more challenging and less relevant to the capsule regimes of interest, we can anticipate that significantly stiffer or more flexible capsules will necessarily respond differently.

The $\zeta(t)$ amplification, shown for the wide and dense case ($W = 40r_0$ and $\phi = 0.7$) in Fig. 21, is altered by the capsule stiffness, but not fundamentally changed. The delays observed for larger Ca reflect changes in the strain energy of the corresponding disturbances. To quantify this, we define strain energy

$$\psi = \frac{\mathcal{T}}{2} \int_{\text{all } C} \left(\frac{ds}{ds_0} - 1 \right)^2 dl + \frac{\mathcal{M}}{2} \int_{\text{all } C} \kappa^2 dl, \qquad (27)$$

and following (8) we define a perturbation value $\psi'(t) \equiv \psi(t) - \psi_b$. Figure 21(b) shows that for stiffer capsules (smaller Ca), the energy of the most transiently amplified initial disturbance for that time, which we designate $\vec{\mathbf{v}}_\zeta(t)$, is nearly constant. However, at a later time, it drops to a value near that of $\vec{\mathbf{s}}_\alpha$. For increasingly flexible capsules, this switch occurs increasingly close to the time when asymptotic amplification is predicted to become significant. In all cases it is clear that the transient disturbances carry significantly more strain energy than the asymptotic ones, indicating that mechanical coupling within the capsules is a key factor only in transient amplification.

VIII. SUMMARY AND CONCLUSIONS

The primary conclusion is that both asymptotic and transient linear amplification of small disturbances can upset single-file trains of flexible capsules when they are not tightly confined. This was confirmed by direct comparison with corresponding nonlinear simulations. Analysis of their growth rates anticipates that transiently amplifying finite, though still small (e.g., $\hat{\varepsilon} = 0.01r_0$), disturbances can significantly accelerate transition to an apparently chaotic flow. Both transiently and asymptotically most-amplified disturbances reach this condition well before the *ad hoc* random disturbances considered, which implies that some sort of stability analysis is necessary to predict transition times in, say, a noisy environment. Interestingly, despite empirical observations of apparently indefinite persistence, capsule trains in a highly confining very narrow channel were also found to be linearly unstable. However, in this case nonlinear effects become active at relatively small displacement amplitudes and preserve the regular train formation.

An implication for the design of devices that process flexible capsules is that channel geometry and packing fraction both significantly affect the most-amplifying disturbances. Qualitatively different most-amplifying disturbances were found to grow at very different rates in different cases. Since the very narrowest channels provide the most obviously persistent capsule trains, it was particularly unexpected that the relatively narrow $W = 10r_0$ channel was significantly more amplifying than the corresponding wider $W = 40r_0$ channel. Yet despite this amplification, for small packing fractions ($\phi = 0.2$) nonlinear effects did not lead to a chaotic seeming flow in the times simulated. Perturbations grew rapidly, but only developed into an irregular single-file arrangement, not the more complicated overturning and passing seen for the more dense configurations.

There are three simplifications in the model configuration studied that warrant additional discussion. The most obvious concerns how well these observations reflect three-dimensional capsule flow. While the two-dimensional model reproduces the same basic phenomenology of three-dimensional systems and has the advantage of requiring little computational effort to explore large ranges of parameters, it is not expected to provide a quantitative model of real systems. Numerical tools to do this are available [3], though subsequent analyses will likely be restricted to a narrower range of parameters. The present study likewise neglects inertia. Though this is undoubtedly a reasonable approximation for many phenomena at these conditions, the Reynolds number might not always be so small as to preclude the accumulation of nonlinear effects at longer

times. However, given the reliance of the present analysis on the boundary integral description of the flow, including inertia in detail would necessitate a substantial redesign of the numerical approach. The third simplification is the matching of the interior capsule viscosity to that of the suspending fluid. It is understood that larger interior viscosities, such as in blood cells, can make them more prone to tumbling, which becomes effectively solid-body motion in the infinite-interior-viscosity limit. We have not investigated this for simplicity, though there is no expectation of any fundamental changes for modest variations of interior viscosity.

Finally, it is unfortunate that the neglect of inertia (and kinetic energy), which makes flow in the viscous limit relatively tractable analytically, precludes a convenient and unique mechanical energy instability metric, such as that available for higher-Reynolds-number incompressible flows. As such, some most-amplifying disturbances have seemingly negligible strain energy, whereas others have significantly more. However, the basic behavior of the instabilities is insensitive to the stiffness of the capsules, so the qualitative response is unchanged by the initial strain energy. The transient amplification is increased for stiffer capsules, as expected, and the switchover to the long-time asymptotic behavior is likewise accelerated, but qualitatively unchanged. The long-time asymptotic stability is relatively insensitive to capsule stiffness for the range considered, presumably because it hinges mostly on the linear flow and the capsule-capsule interaction mechanics it mediates. There is an abrupt switch between the short-time behavior, for which the most-dangerous perturbations carry relatively large strain energy, and the asymptotically most unstable modes, which do not.

[1] R. Skalak and P. I. Branemark, Deformation of red blood cells in capillaries, Science **164**, 717 (1969).

[2] A. R. Pries and T. W. Secomb, Rheology of the microcirculation, Clin. Hemorheol. Microcirc. **29**, 143 (2003).

[3] J. B. Freund, Numerical simulations of flowing blood cells, Annu. Rev. Fluid Mech. **46**, 67 (2014).

[4] B. Kaoui, G. Biros, and C. Misbah, Why do Red Blood Cells have Asymmetric Shapes Even in a Symmetric Flow? Phys. Rev. Lett. **103**, 188101 (2009).

[5] H. Noguchi and G. Gompper, Shape transitions of fluid vesicles and red blood cells in capillary flows, Proc. Natl. Acad. Sci. USA **102**, 14159 (2005).

[6] H. Schmid-Schönbein and P. Gaehtgens, What is red-cell deformability? Scand. J. Clin. Lab. Inv. **41**, 13 (1981).

[7] G. Tomaiuolo, M. Simeone, V. Martinelli, B. Rotoli, and S. Guido, Red blood cell deformation in microconfined flow, Soft Matter **5**, 3736 (2009).

[8] P. Gaehtgens, C. Duhrssen, and K. H. Albrecht, Motion, deformation, and interaction of blood cells and plasma during flow through narrow capillary tubes, Blood Cells **6**, 799 (1980).

[9] T. M. Griffith, Temporal chaos in the microcirculation, Cardiovascular Res. **31**, 342 (1996).

[10] K. D. Barclay, G. A. Klassen, and C. Young, A method for detecting chaos in canine myocardial microcirculatory red cell flux, Microcirculation **7**, 335 (2000).

[11] H. Zhao, A. H. G. Isfahani, L. Olson, and J. B. Freund, A spectral boundary integral method for microcirculatory cellular flows, J. Comput. Phys. **229**, 3726 (2010).

[12] H. Zhao and E. S. G. Shaqfeh, The dynamics of a non-dilute vesicle suspension in a simple shear flow, J. Fluid Mech. **725**, 709 (2013).

[13] P. Bagchi and R. M. Kalluri, Rheology of a dilute suspension of liquid-filled elastic capsules, Phys. Rev. E **81**, 056320 (2010).

[14] D. A. Fedosov, M. Dao, G. E. Karniadakis, and S. Suresh, Computational biorheology of human blood flow in health and disease, Ann. Biomed. Eng. **42**, 368 (2013).

[15] H. Aref, Stirring by chaotic advection, J. Fluid Mech. **143**, 1 (1984).

[16] J. M. Ottino, *The Kinematics of Mixing: Stretching, Chaos and Transport* (Cambridge University Press, Cambridge, 1989).

[17] K. Bajer and H. K. Moffatt, On a class of steady confined Stokes flows with chaotic streamlines, J. Fluid Mech. **212**, 337 (1990).

[18] H. A. Stone, A. Nadim, and S. H. Strogatz, Chaotic streamlines inside drops immersed in steady Stokes flows, J. Fluid Mech. **232**, 629 (1991).

[19] D. Kroujiline and H. A. Stone, Chaotic streamlines in steady bounded three-dimensional Stokes flows, Physica D **130**, 105 (1999).

[20] I. M. Jánosi, T. Tél, D. E. Wolf, and J. A. C. Gallas, Chaotic particle dynamics in viscous flows: The three-particle Stokeslet problem, Phys. Rev. E **56**, 2858 (1997).

[21] T. Mullin, Y. Li, C. D. Pino, and J. Ashmore, An experimental study of fixed points and chaos in the motion of spheres in a Stokes flow, IMA J. Appl. Math. **70**, 666 (2005).

[22] A. S. Popel, Theory of oxygen transport to tissue, Crit. Rev. Biomed. Eng. **17**, 257 (1989).

[23] C. Pozrikidis, Numerical simulation of blood flow through microvascular capillary networks, Bull. Math. Biol. **71**, 1520 (2009).

[24] C. Alonso, A. R. Pries, O. Kiesslich, D. Lerche, and P. Gaehtgens, Transient rheological behavior of blood in low-shear tube flow: velocity profile and effective viscosity, Am. J. Physiol. Heart Circ. Physiol. **268**, 25 (1995).

[25] M. Soutani, Y. Suzuki, and N. Maeda, Quantitative evaluation of flow dynamics of erythrocytes in microvessels: Influence of erythrocyte aggregation, Am. J. Physiol. Heart Circ. Physiol. **268**, H1959 (1995).

[26] S. Kim, P. K. Ong, O. Yalcin, M. Intaglietta, and P. C. Johnson, The cell-free layer in microvascular blood flow, Biorheology **46**, 181 (2009).

[27] J. C. Firrell and H. H. Lipowsky, Leukocyte margination and deformation in mesenteric venules of ram, Am. J. Physiol. Heart Circ. Physiol. **225**, 1667 (1989).

[28] J. B. Freund, Leukocyte margination in a model microvessel, Phys. Fluids **19**, 023301 (2007).

[29] H. Zhao and E. S. G. Shaqfeh, Shear-induced platelet margination in a microchannel, Phys. Rev. E **83**, 061924 (2011).

[30] A. Kumar, R. G. H. Rivera, and M. D. Graham, Flow-induced segregation in confined multicomponent suspensions: Effects of particle size and rigidity, J. Fluid Mech. **738**, 423 (2014).

[31] R. G. H. Rivera, K. Sinha, and M. D. Graham, Margination Regimes and Drainage Transition in Confined Multicomponent Suspensions, Phys. Rev. Lett. **114**, 188101 (2015).

[32] J. B. Freund, J. Goetz, K. Hill, and J. Vermot, Fluid flows and forces in development: Functions, features and biophysical principles, Development **139**, 1229 (2012).

[33] T. W. Secomb, J. P. Alberding, R. Hsu, M. W. Dewhirst, and A. R. Pries, Angiogenesis: An adaptive dynamic biological patterning problem, PLoS Comput. Biol. **9**, e1002983 (2013).

[34] J. B. Freund and J. Vermot, The wall-stress footprint of blood cells flowing in microvessels, Biophys. J. **106**, 752 (2014).

[35] F. Boselli, J. B. Freund, and J. Vermot, Blood flow mechanics in cardiovascular development, Cell. Mol. Life Sci. **72**, 2545 (2015).

[36] P. Koumoutsakos, I. Pivkin, and F. Milde, The fluid mechanics of cancer and its therapy, Annu. Rev. Fluid Mech. **45**, 325 (2013).

[37] C. Galligan, J. Nichols, E. Kvam, P. Spooner, R. Gettings, L. Zhu, and C. M. Puleo, Mesoscale blood cell sedimentation for processing millilitre sample volumes, Lab Chip **15**, 3274 (2015).

[38] N. Xiang and Z. Ni, High-throughput blood cell focusing and plasma isolation using spiral inertial microfluidic devices, Biomed. Microdevices **17**, 110 (2015).

[39] J. Choi, J. Hyun, and S. Yang, On-chip extraction of intracellular molecules in white blood cells from whole blood, Sci. Rep. **5**, 15167 (2005).

[40] M. Abkarian, M. Faivre, R. Horton, K. Smistrup, and C. Best-Popescu, Cellular-scale hydrodynamics, Biomed. Mater. **3**, 034011 (2008).

[41] M. Toner and D. Irimia, Blood-on-a-chip, Annu. Rev. Biomed. Eng. **7**, 77 (2005).

[42] J. Kim, M. Massoudi, J. F. Antaki, and A. Gandini, Removal of malaria-infected red blood cells using magnetic cell separators: A computational study, Appl. Math. Comput. **218**, 6841 (2012).

[43] T. W. Secomb, R. Skalak, N. Ozkaya, and J. F. Gross, Flow of axisymmetric red blood cells in narrow capillaries, J. Fluid Mech. **163**, 405 (1986).

[44] J. B. Freund and M. M. Orescanin, Cellular flow in a small blood vessel, J. Fluid Mech. **671**, 466 (2011).

[45] J. L. McWhirter, H. Noguchi, and G. Gompper, Ordering and arrangement of deformed red blood cells in flow through microcapillaries, New J. Phys. **14**, 085026 (2012).

[46] P. J. Schmid and D. S. Henningson, *Stability and Transition in Shear Flows* (Springer, Berlin, 2012).

[47] P. J. Schmid, Nonmodal stability theory, Annu. Rev. Fluid Mech. **39**, 129 (2007).

[48] M. Zhang, F. Martinelli, J. Wu, P. J. Schmid, and M. Quadrio, Modal and non-modal stability analysis of electrohydrodynamic flow with and without cross-flow, J. Fluid Mech. **770**, 319 (2015).

[49] S. C. Reddy and D. S. Henningson, Energy growth in viscous channel flows, J. Fluid Mech. **252**, 209 (1993).

[50] J. M. Crowley, Viscosity-induced instability of a one-dimensional lattice of falling spheres, J. Fluid Mech. **45**, 151 (1971).

[51] L. M. Hocking, The behavior of clusters of spheres falling in a viscous fluid, J. Fluid Mech. **20**, 129 (1964).

[52] S. L. Goren, Resistance and stability of a line of particles moving near a wall, J. Fluid Mech. **132**, 185 (1983).

[53] M. R. Jovanovic and S. Kumar, Nonmodal amplification of stochastic disturbances in strongly elastic channel flows, J. Non-Newtonian Fluid Mech. **166**, 755 (2011).

[54] T. Beatus, T. Tlusty, and R. Bar-Ziv, Phonons in a one-dimensional microfluidic crystal, Nat. Phys. **2**, 743 (2006).

[55] J. Fleury, U. D. Schiller, S. Thutupalli, G. Gompper, and R. Seemann, Mode coupling of phonons in a dense one-dimensional microfluidic crystal, New J. Phys. **16**, 063029 (2014).

[56] U. D. Schiller, J. Fleury, R. Seemann, and G. Gompper, Collective waves in dense and confined microfluidic droplet arrays, Soft Matter **11**, 5850 (2015).

[57] S. Kuriakose and P. Dimitrakopoulos, Deformation of an elastic capsule in a rectangular microfluidic channel, Soft Matter **9**, 4284 (2013).

[58] D. Obrist and P. J. Schmid, On the linear stability of swept attachment-line boundary layer flow. Part 2. Non-modal effects and receptivity, J. Fluid Mech. **493**, 31 (2003).

[59] L. Brandt, C. Cossu, J. M. Chomaz, P. Huerre, and D. S. Henningson, On the convectively unstable nature of optimal streaks in boundary layers, J. Fluid Mech. **485**, 221 (2003).

[60] P. Corbett, Nonmodal growth in boundary layers and its optimal control, Ph.D. thesis, Ecole Polytechnique Fédérale de Lausanne, 2000.

[61] J. Kim and T. R. Bewley, A linear systems approach to flow control, Annu. Rev. Fluid Mech. **39**, 383 (2007).

[62] T. R. Bewley, Flow control: New challenges for a new renaissance, Prog. Aerosp. Sci. **37**, 21 (2001).

[63] H. Hogberg, T. R. Bewley, and D. S. Henningson, Linear feedback control and estimation of transition in plane channel flow, J. Fluid Mech. **481**, 149 (2001).

[64] N. Hoda, M. R. Jovanovic, and S. Kumar, Energy amplification in channel flows of viscoelastic fluids, J. Fluid Mech. **601**, 407 (2008).

[65] J. Klinkenberg, H. de Lange, and L. Brandt, Modal and non-modal stability of particle-laden channel flow, Phys. Fluids **23**, 064110 (2011).

[66] S. H. Bryngelson and J. B. Freund, Buckling and its effect on the confined flow of a model capsule suspension, Rheol. Acta **55**, 451 (2016).

[67] I. Cantat and C. Misbah, Lift Force and Dynamical Unbinding of Adhering Vesicles Under Shear Flow, Phys. Rev. Lett. **83**, 880 (1999).

[68] L. Distenfass, Internal viscosity of the red cell and a blood viscosity equation, Nature (London) **219**, 956 (1968).

[69] J. D. Bronzino, *The Biomedical Engineering Handbook* (IEEE/CRC, Boca Raton, 2000).

[70] G. Danker, P. M. Vlahovska, and C. Misbah, Vesicles in Poiseuille Flow, Phys. Rev. Lett. **102**, 148102 (2009).

[71] J. B. Freund and H. Zhao, *Hydrodynamics of Capsules and Biological Cells* (Chapman and Hall/CRC, Boca Raton, 2010), pp. 71–111.

[72] C. Pozrikidis, *Boundary Integral and Singularity Methods for Linearized Viscous Flow* (Cambridge University Press, Cambridge, 1992).

[73] S. Kim and S. J. Karrila, *Microhydrodynamics: Principles and Selected Applications* (Butterworth-Heinemann, Boston, 1991).

[74] E. Metsi, Large scale simulations of bidisperse emulsions and foams, Ph.D. thesis, University of Illinois at Urbana–Champaign, 2000.

[75] H. Hasimoto, On the periodic fundamental solutions of the Stokes equations and their application to viscous flow past a cubic array of spheres, J. Fluid Mech. **5**, 317 (1959).

[76] L. Trefethen and M. Embree, *Spectra and Pseudospectra: The Behavior of Nonnormal Matrices and Operators* (Princeton University Press, Princeton, 2005).

[77] G. I. Barenblatt, *Scaling, Self-Similarity, and Intermediate Asymptotics* (Cambridge University Press, Cambridge, 1996).

[78] L. Preziosi, K. Chen, and D. D. Joseph, Lubricated pipelining: Stability of core-annular flow, J. Fluid Mech. **201**, 323 (1989).

[79] H. H. Hu and D. D. Joseph, Lubricated pipelining: Stability of core-annular flow: Part 2, J. Fluid Mech. **205**, 359 (1989).

[80] G. Tomaiuolo, L. Lanotte, G. Ghigliotti, C. Misbah, and S. Guido, Red blood cell clustering in poiseuille microcapillary flow, Phys. Fluids **24**, 051903 (2012).

[81] J. L. McWhirter, H. Noguchi, and G. Gompper, Flow-induced clustering and alignment of vesicles and red blood cells in microcapillaries, Proc. Natl. Acad. Sci. USA **106**, 6039 (2009).